Computed laminography and reconstruction algorithm

QUE Jie-Min(阙介民)[1,2,3] CAO Da-Quan(曹大泉)[1,2,3] ZHAO Wei(赵维)[1,2,3]
TANG Xiao (唐晓)[1,2,3] SUN Cui-Li(孙翠丽)[1,2] WANG Yan-Fang(王燕芳)[1,2]
WEI Cun-Feng(魏存峰)[1,2] SHI Rong-Jian(史戎坚)[1,2] WEI Long(魏龙)[1,2]
YU Zhong-Qiang(郁忠强)[1,2] YAN Yong-Lian(阎永廉)[1,2]

[1] Institute of High Energy Physics, Chinese Academy of Sciences, Beijing 100049, China
[2] Research Center of Radiation Imaging Technology and Facilities Engineering Technology of Beijing, Beijing 100049, China
[3] Key Laboratory of Nuclear Analytical Techniques, Chinese Academy of Sciences, Beijing 100049, China

Abstract: Computed laminography (CL) is an alternative to computed tomography if large objects are to be inspected with high resolution. This is especially true for planar objects. In this paper, we set up a new scanning geometry for CL, and study the algebraic reconstruction technique (ART) for CL imaging. We compare the results of ART with variant weighted functions by computer simulation with a digital phantom. It proves that ART algorithm is a good choice for the CL system.

Key words: computed laminography (CL), ART, weighted function

PACS: 81.70.Tx **DOI:** 10.1088/1674-1137/36/8/017

1 Introduction

Computed tomography (CT) is a well-established technique for non-destructive testing and evaluation. However, when large objects are to be inspected with high spatial resolution CT has limitations, especially for planar objects. CT requires the object to be imaged from many directions around a circle. This is not possible for extended objects either due to geometrical restrictions or high absorption of X-rays in certain directions. In these cases computed laminography (CL) provides a viable alternative to CT [1]. CL has been used for the inspection of printed circuit boards for several years.

The geometry of tomographic measurements is different from laminographic measurement. In a tomography system, the central X-ray beam is perpendicular to the sample rotation axis, while in a laminography system, the central X-ray beam has a certain tilt angle with the detector. This scan geometry is suitable for objects with limited access to all viewing angles, especially for planar objects such as printed circuit boards. For this reason, CL is widely used in non-destructive testing areas. CL was first proposed in 1916 and has been extensively investigated since then. In China, YANG Min et al. first introduced the CL method for the Non-Destructive testing of shell-like or plate-like objects in 2003 [2]. In 2010, FU Jian et al. developed an experimental CL system, and discussed the two pre-processing methods for projection to improve the quality of image reconstructed by ART algorithm, then verified the validity of the method by experiments [3]. FU Jian et al. introduced a large field of view computed laminography with the asymmetric rotational scanning geometry, the filtered back-projection (FBP) reconstruction algorithm and the data truncation smoothing functions were deduced to reconstruct the images directly from the data acquired with this asymmetric configuration, and the results confirmed that the proposed method can enlarge the imaging region and improve the spatial resolution [4].

This paper develops a new CL system with two rotational stages, which can implement both conventional 3D CT scanning and CL scanning. In addition, computer simulation of the scanning process of the

Received 21 November 2011, Revised 16 December 2011

CL system with a digital phantom is performed. The results show that the ART algorithm can significantly reduce the overlap artifacts in the reconstruction images. We also analyze the results reconstructed by ART with the voxel-driven approach and the ray-driven approach which are not shown in previous papers. In Section 2, we describe the scanning geometry and the scanning principle of the method. In Section 3, we present the process of imaging and the reconstruction technique. In Section 4 we show the computer simulation and the comparison of the FBP algorithm and the ART algorithm for CL. In Section 5, we introduce a new CL system and some CL experiments are described to confirm that the results reconstructed by the ART algorithm were better than the results reconstructed by the FBP algorithm. We give a brief discussion and conclusion in Section 6.

2 Description of the CL scanning geometry

There are three scanning geometry types for the CL system: linear, planar and rotational, respectively. The planar geometry is conventional laminography, not suitable for the inspection of large and heavy objects. It requires the precise translation of objects over long distances. The rotational configuration has some advantages over the conventional linear or planar laminography. Only the rotary bearing movement during the scan has a simple geometrical structure and the space requirement is not as high as the other modes. Furthermore, the beam angle of the X-ray tube does not need to be as wide as the conventional laminography. We selected rotational scanning for its short scanning times and improved reconstructed image quality.

The CL scanning geometry is shown in Fig. 1. It consists of three parts: an X-ray source, a two-dimensional digital flat panel detector (FPD), and a rotation gantry. X-ray beams penetrate through an object onto a two-dimensional X-ray detector. By rotating the scanned object or the X-ray cone beam defined by the X-ray source and the detector, a set of projection images are measured and are stored in the computer.

3 The reconstruction technique

FBP is a simple and fast reconstruction technique but it has its drawbacks for CL. The FBP algorithm is suitable for complete projection data. Algebraic methods have many advantages over FBP, such as better noise tolerance and better handling of spare and non-uniformly distributed projection datasets. In this section, we explain the theoretical basics of the FBP algorithm [4] and the ART algorithm.

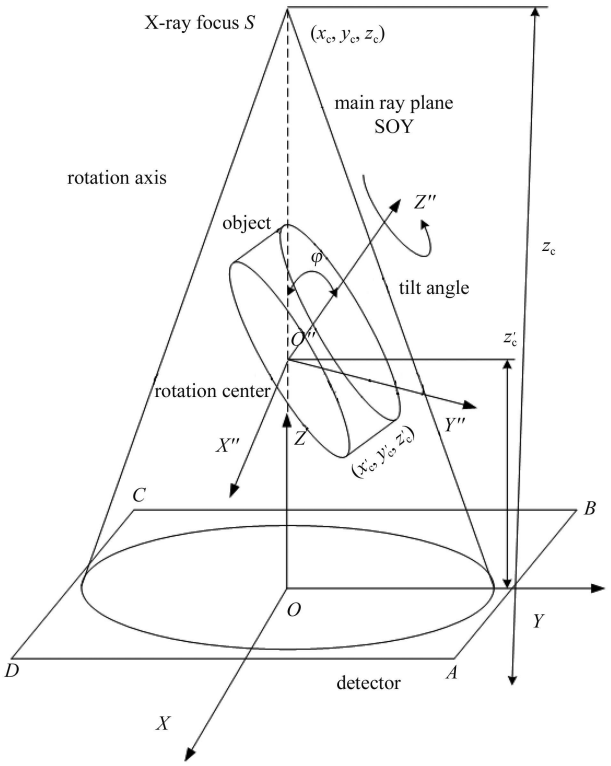

Fig. 1. The CL geometry layout.

For convenient expression, the coordination unification is first executed. As shown in Fig. 1, S is the focus spot of the X-ray source. $ABCD$ is the actual detector. SO is the main X-ray. SOY is the main X-ray plane. The rotation axis Z'' belongs to the plane SOY and intersects with SO at the point O''. Let $f(x'',\ y'',\ z'')$ represent the spatial distribution of the X-ray absorption coefficient. $P(x,y,\theta)$ represent the projection image acquired by detectors as a function of three variables, which is defined as a line integral of $f(x'',\ y'',\ z'')$ along the X-ray beam transmission locus τ specified by X, Y and θ, expressed by Eq. (1). Parameters X and Y denote the positions of the detector channel. θ represents the rotational angle position with respect to the rotational axis Z''. z_c is the distance from the X-ray focal spot to the FPD. z_c' is the distance from the FPD to the rotation center O''.

$$P(X,Y,\theta)=\int_{\tau} f(x'',y'',z'')\mathrm{d}\tau, \tag{1}$$

$$f(x'',y'',z'')=\int_0^{2\pi}\int_{-\infty}^{+\infty} P(X,Y,\theta)h(Y-Y')\mathrm{d}Y\,\mathrm{d}\theta, \tag{2}$$

$$h(Y)=\int_{-\infty}^{+\infty}|\omega|\mathrm{e}^{\mathrm{i}2\pi\omega Y}\mathrm{d}\omega, \tag{3}$$

$$\begin{cases} X=-\dfrac{z_{\mathrm{c}}\cdot(x''\cos\theta+y''\sin\theta)}{x''\sin\theta\sin\varphi-y''\cos\theta\sin\varphi+z''\cos\varphi+z'_{\mathrm{c}}-z_{\mathrm{c}}} \\ Y=-\dfrac{z_{\mathrm{c}}\cdot(-x''\sin\theta\cos\varphi+y''\cos\theta\cos\varphi+z''\sin\varphi)}{x''\sin\theta\sin\varphi-y''\cos\theta\sin\varphi+z''\cos\varphi+z'_{\mathrm{c}}-z_{\mathrm{c}}} \end{cases}, \tag{4}$$

$$[x^*,y^*,z^*,1]=[x'',y'',z'',1]\cdot R_3\cdot R_2\cdot R_1, \tag{5}$$

$$R_3=\begin{bmatrix}\cos\theta & -\sin\theta & 0 & 0\\ \sin\theta & \cos\theta & 0 & 0\\ 0 & 0 & 1 & 0\\ 0 & 0 & 0 & 1\end{bmatrix},$$

$$R_2=\begin{bmatrix}1 & 0 & 0 & 0\\ 0 & \cos\varphi & -\sin\varphi & 0\\ 0 & \sin\varphi & \cos\varphi & 0\\ 0 & 0 & 0 & 1\end{bmatrix},$$

$$R_1=\begin{bmatrix}1 & 0 & 0 & 0\\ 0 & 1 & 0 & 0\\ 0 & 0 & 1 & 0\\ x'_{\mathrm{c}} & y'_{\mathrm{c}} & z'_{\mathrm{c}} & 1\end{bmatrix},$$

$$\begin{cases} x^*=x''\cos\theta+y''\sin\theta+x'_{\mathrm{c}} \\ y^*=-x''\sin\theta\cos\varphi+y''\cos\theta\cos\varphi+z''\sin\varphi+y'_{\mathrm{c}} \\ z^*=x''\sin\theta\sin\varphi-y''\cos\theta\sin\varphi+z''\cos\varphi+z'_{\mathrm{c}} \end{cases}, \tag{6}$$

$$\frac{x-x_{\mathrm{c}}}{x^*-x_{\mathrm{c}}}=\frac{y-y_{\mathrm{c}}}{y^*-y_{\mathrm{c}}}=\frac{z-z_{\mathrm{c}}}{z^*-z_{\mathrm{c}}}=t, \tag{7}$$

$$z=0, \tag{8}$$

$$\begin{cases} X=x=\dfrac{x_{\mathrm{c}}\cdot z^*-z_{\mathrm{c}}\cdot x^*}{z^*-z_{\mathrm{c}}} \\ Y=y=\dfrac{y_{\mathrm{c}}\cdot z^*-z_{\mathrm{c}}\cdot y^*}{z^*-z_{\mathrm{c}}} \end{cases}, \tag{9}$$

$$x_{\mathrm{c}}=0,\ y_{\mathrm{c}}=0,\ x'_{\mathrm{c}}=0,\ y'_{\mathrm{c}}=0. \tag{10}$$

The back-projection addresses of X and Y with all the rotation angles have been calculated by Eq. (4). Here we show the procedure to deduce Eq. (5). Eq. (5) gives the coordinate transform relationship between $X''Y''Z''$and XYZ. The reconstructed point (x'', y'', z'') can be represented by (x^*,y^*,z^*) in the coordinate system XYZ with Eqs. (5) and (6). Eq. (7) represents the X-ray beam through the reconstructed point (x^*, y^*, z^*). Eq. (8) represents the detector plane. According to Eqs. (6)–(8), we can get the back-projection address calculation Eq. (9). Using Eq. (10) we can simplify Eq. (4). Eq. (2) shows the FBP algorithm for the geometry. Eq. (3) is the filter function of the FBP algorithm. Shepp-Logan function is the common filter for FBP.

The ART algorithm processes one element of $f(x'',\ y'',\ z'')$, i.e. f_j can be expressed by:

$$f_j^{(k+1)}=f_j^{(k)}+\lambda\frac{P_i-\sum_{n=1}^{N}w_{\mathrm{in}}f_{\mathrm{n}}^k}{\sum_{n=1}^{N}w_{\mathrm{in}}^2}w_{ij}, \tag{11}$$

where λ is the relaxation factor typically chosen within the interval (0.0, 1.0], but usually much less than 1.0 to dampen the correction overshoot. w_{in} is the weight coefficient which represents a measure of the influence that voxel f_{n} has on the ray r_i passing through pixel P_i. It is clear that the weight coefficients bear a crucial role in the solution of this equation. They are the elements that link the unknown voxel values to the known detector pixel values. In order to get the accurate solution, each weight w_{ij} must accurately represent the influence of a voxel f_j on the ray r_j passing through pixel P_i. Generally, the weight coefficients are calculated by the interpolation kernel function, such as box function, bilinear function, Gaussian function and Bessel-Kaiser function [5].

Implementations of back-projection for FBP reconstruction usually use a pixel-driven or voxel-driven approach, while implementations of back-projection for ART reconstruction can use a voxel-driven approach and ray-driven approach. Voxel-driven back-projection works by connecting a ray line from the focal spot through the center of the pixel of the detector. Once a location of intersection on the detector is calculated, a value is obtained from the detector by (typically linear) interpolation, and the result is accumulated in the pixel. Ray-driven projection works by connecting a line from the focal spot through the image to the center of the detector cell of interest. For every image row (or column), a location of intersection is calculated, a value is obtained from the image row, typically by linear interpolation, and the result is calculated in the detector cell [6]. Eqs. (4)–(11) is the process of the voxel-driven back-projection approach. The following equation gives the process of a ray-driven back-projection approach. The focal

spot point in the coordinate $X''Y''Z''$ is represented by Eq. (12). The detector cell point (x_i, y_i, 0) in the coordinate XYZ is represented by Eq. (13) in the coordinate $X''Y''Z''$. We can get the ray beam point intersected the object in the coordinate $X''Y''Z''$ by Eqs. (12), (13) and (14).

$$\begin{cases} x''_{\rm c} = (z_{\rm c} - z'_{\rm c}) \cdot \sin\theta \cdot \sin\varphi \\ y''_{\rm c} = -(z_{\rm c} - z'_{\rm c}) \cdot \cos\theta \cdot \sin\varphi \\ z''_{\rm c} = (z_{\rm c} - z'_{\rm c}) \cdot \cos\varphi \end{cases}, \tag{12}$$

$$\begin{cases} x''_i = x_i \cdot \cos\theta - y_i \cdot \sin\theta \cdot \cos\varphi + (0 - z'_{\rm c}) \cdot \sin\theta \cdot \sin\varphi \\ y''_i = x_i \cdot \sin\theta + y_i \cdot \cos\theta \cdot \cos\varphi - (0 - z'_{\rm c}) \cdot \cos\theta \cdot \sin\varphi \\ z''_i = y_i \cdot \sin\varphi + (0 - z'_{\rm c}) \cdot \cos\varphi \end{cases}, \tag{13}$$

$$z'_{\rm c} = 0, \tag{14}$$

$$t_i = \frac{z'' - z_{\rm c} \cdot \cos\varphi}{y_i \cdot \sin\varphi - z_{\rm c} \cos\varphi}, \tag{15}$$

$$\begin{cases} x'' = z_{\rm c} \cdot \sin\theta \cdot \sin\varphi + (x_i \cdot \cos\theta - y_i \cdot \sin\theta \cdot \cos\varphi - z_{\rm c} \cdot \sin\theta \cdot \sin\varphi) \cdot t_i \\ y'' = -z_{\rm c} \cdot \cos\theta \cdot \sin\varphi + (x_i \cdot \sin\theta + y_i \cdot \cos\theta \cdot \cos\varphi + z_{\rm c} \cdot \cos\theta \cdot \sin\varphi) \cdot t_i \\ z'' = \text{the } i \text{ slice} \end{cases}. \tag{16}$$

Eq. (14) is used to simplify calculation. Then the reconstructed voxel point is magnified $z_{\rm c}/z'_{\rm c}$ multiple. Eqs. (14)–(16) can confirm the reconstructed voxel point through the projection on the detector.

4 The computer simulation and analysis

In this section we compare the results of ART algorithm with different interpolation methods and the results of FBP for the phantom in Fig. 2. The phantom consists of a big cylinder and it includes six small cylinders with different diameter and height. The parameters of this phantom are listed in Table 1. The simulation parameters for the scanning geometry are listed below (unit: pixel);

$$z_{\rm c} = 800,\ z'_{\rm c} = 200,\ \varphi = 45^\circ,$$
$${\rm d}\theta = 6^\circ,\ N = 128,\ AB = 128,\ AD = 128.$$

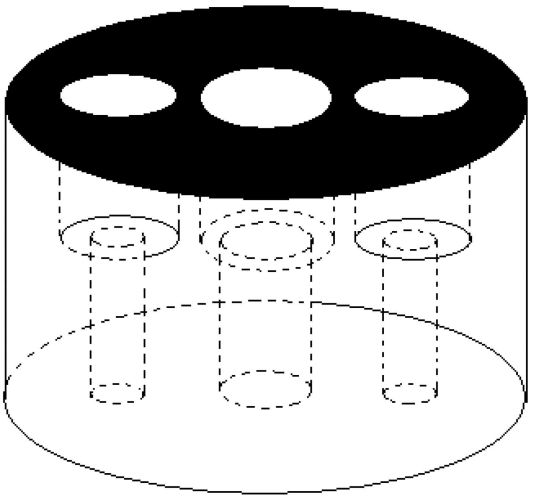

Fig. 2. The simulation phantom (refer to Table 1 for the details).

Table 1. The parameters of the phantom.

No.	center coordinates (x, y)		height(z)		radius	attenuation coefficient/cm^{-1}
			start	end		
1	0	0	0	20	40	0.2
2	−20	0	10	20	6	0
3	0	0	10	20	10	0
4	0	20	10	20	6	0
5	−20	0	0	10	4	0
6	0	0	0	10	6	0
7	0	20	0	10	4	0

With the above geometry, the projection data is firstly generated by the discrete implementation of Eq. (1) based on the X-ray attenuation Beer-Lambert law of the materials and the simulation parameters. The implementation includes the following steps. (1) Construct the mathematical models of the cylinders and the X-ray beam in the 3D space. (2) Solve the intersection points between cylinders and the X-ray beam according to the models. (3) Calculate the X-ray path length through the cylinders according to the intersection points. (4) Get the projection data by multiplying the length with X-ray attenuation coefficient of the cylinders.

Figure 3 shows the image reconstructed by Eqs. (2) and (11). From Fig. 3, we can find the FBP algorithm brings obvious overlap artifacts. The results reconstructed with ART algorithm are much better than the results reconstructed with FBP algorithm. While the gray value of the image reconstructed by ART is closer to the actual value than it reconstructed by FBP because the image reconstructed by FBP is accumulated by all projection. CL can not meet the necessary and sufficient condition for the conventional CT reconstruction proposed by Tuy [7]. The number projection which FBP needed is twice that of ART [8]. ART can add prior information in the correction.

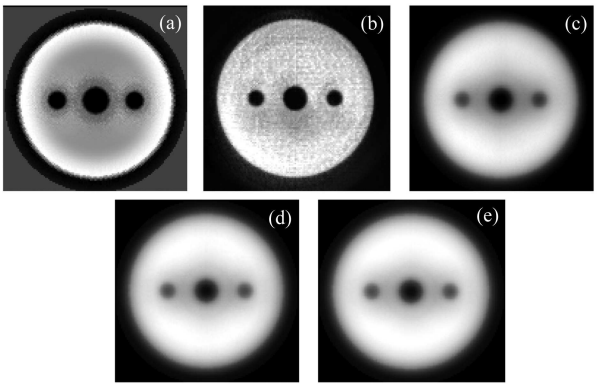

Fig. 3. Results of variant methods. (a) FBP; (b) ART with box function; (c) ART with bilinear function; (d) ART with Gaussian function; (e) ART with Bessel-Kaiser function.

In order to verify the effect of the accuracy of the interpolation function on the reconstructed images, we compare the various over-sampled box functions for ART. Fig. 4(a)–(d) shows the results of ART with different over-sampled box functions. From the results, we can deduce that the more accurate the weighted value, the better the image reconstructed with ART.

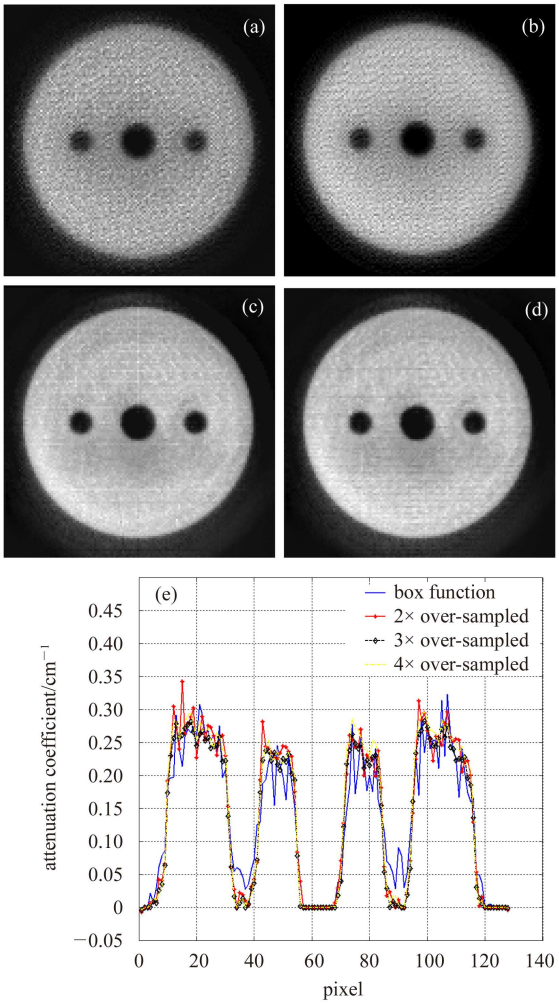

Fig. 4. The comparison of the reconstructed image by the ART algorithm with various over-sampled box functions. (a) Box function; (b) 2× over-sampled; (c) 3× over-sampled; (d) 4× over-sampled; (e) The comparison of the corresponding gray value curves at the same row of the image reconstructed by ART with various over-sampled box function.

5 The system and experiments

In this section, we check the validity of the advantage of ART algorithm with experiments. We have developed a CL imaging system on the basis of a conventional cone-beam CT system. We have added a rotation stage in which its center axes are perpendicular to the former rotation stage center axes. The geometry ensures that the conventional scanning function and the CL scanning could be carried out. It consists of a 225 kV X-ray source from COMET Company, a FPD PaxScan2520 from Varian Company (USA), an optical table and two rotation stages. The size of the detector pixel is 0.127 mm and the length of the

detector is about 250 mm and the height is 200 mm. Fig. 5 shows the CL system.

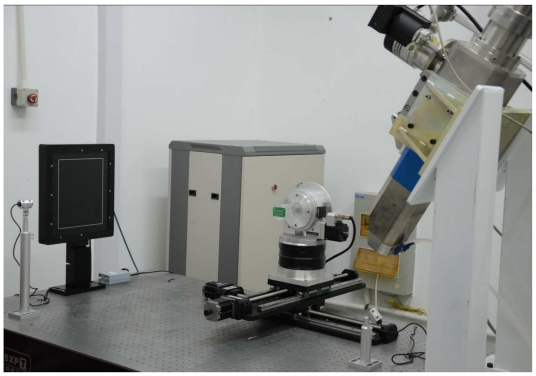

Fig. 5. The developed CL system.

A circuit board is selected to be the test specimen. The imaging conditions for the circuit board are listed below:

$Z_c = 1260$ mm, Z'_c=600 mm, $\varphi = -45°$, $d\theta = 1°$, $N = 1024$ pixels, $AB = 1920$ pixels, $AD = 1536$ pixels.

Figure 6 is the photo of the circuit board. Fig. 7 shows the projection images with different scan angles. Fig. 8 shows the CL slice images reconstructed by the FBP algorithm and ART algorithm.

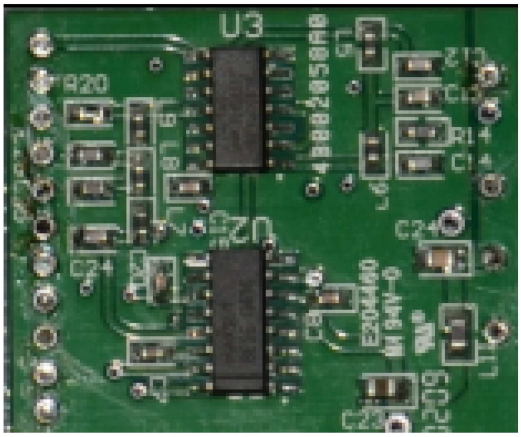

Fig. 6. The photo of a circuit board.

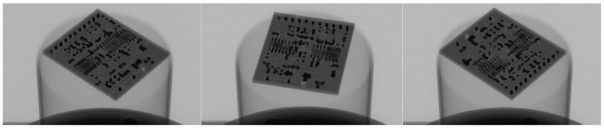

Fig. 7. The projection images of the circuit board with different scan angles.

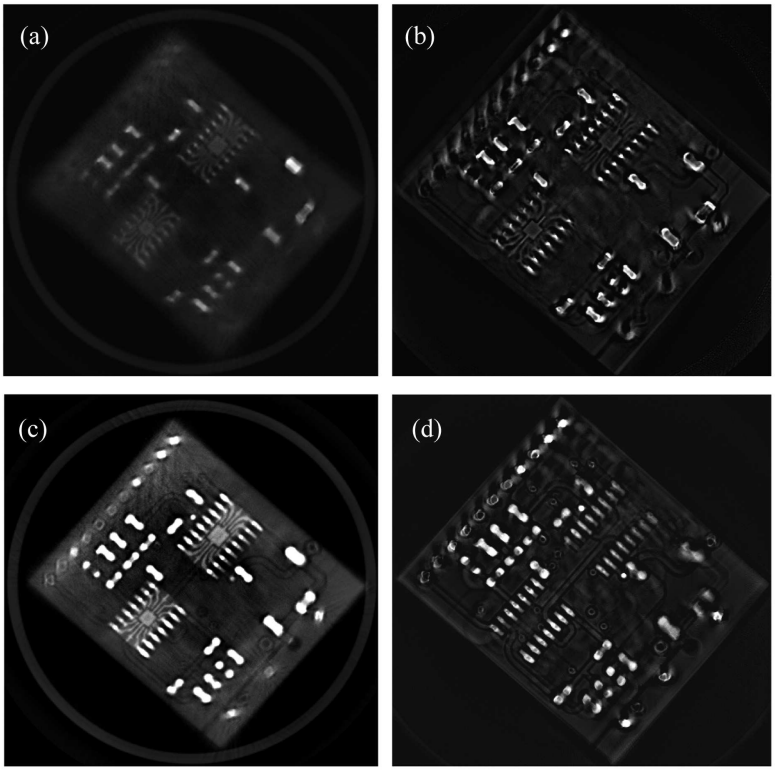

Fig. 8. The CL imaging results of the printed circuit board. (a) FBP (slice 1); (b) ART (slice 1); (c) FBP (slice 5); (d) ART (slice 5).

For convenient display, the background area of all the reconstructed images have been cut off and the gray level has been adjusted to the same level compared. From Fig. 8 (c) and (d), we can find the image reconstructed by FBP is much smoother than by ART, but the detail in the image reconstructed by ART is clearer than by FBP. On Fig. 8 (c), the information of another slice is shown at the edge of the image reconstructed by FBP. From the results, we can see that the reconstructed images by FBP algorithm have more overlap artifacts than by the ART algorithm. So the ART algorithm is more advantageous for CL system imaging.

6 Discussion and conclusion

In this paper we have developed a new CL scanning system. In addition, we have compared the ART reconstruction algorithm and the FBP algorithm with numerical studies and experiments. Compared to the conventional analytical algorithm, it is proved that the ART algorithm can significantly reduce the overlap artifacts in the CL system, while the ART reconstruction algorithm needs more time than the FBP algorithm. Future work will concentrate on enhancing the reconstruction speed. We will adopt the graphics process units(GPU) to accelerate the speed of reconstruction [9, 10]. Furthermore, we compared the results of ART with various interpolation functions. We have found that the Bessel-Kaiser function and over-sampled box function are good choices for ART algorithm. The process of ART affects the quality of the reconstructed image. The voxel-driven approach produces high frequency noise, but the ray-driven approach has none.

We are grateful to the referee, whose comments led to the improvement of this paper. We also wish to express our thanks to the Imaging Engineering Group for useful discussion and especially to ZHAO Wei for technical support.

References

1 Maisl M, Porsch F, Schorr C. Computed Laminography for X-ray Inspection of Light- weight Construction. 2nd International Symposium on NDT in Aerospace 2010-M0.3.A3
2 YANG Min，LU Hong-Nian，ZHANG Ya-Chong. Journal of Xi'an Jiaotong University, 2003, **37**(3): 245–248 (in Chinese)
3 FU Jian, WANG Hong-Jun, LI Bin, JIANG Bai-Hong. Acta Electronica Sinica, 2010, **38**(7): 1580–1584 (in Chinese)
4 FU Jian, JIANG Bai-Hong, LI Bin. Sci. China Tech. Sci., 2010, **53**(8): 2261–2271 (in Chinese)
5 Mueller K, Yagel R, Wheller J J. IEEE Transactions on Medical Imaging, 1999, **18**(6): 538–548
6 de Man B, Basu S. Phys. Med. Biol., 2004, **49**: 2463–2475
7 Tuy H K. SIAM J Appl. Math., 1983, **43**: 546–552
8 Guan H, Gordon R. Phys. Med. Biol., 1996, **41**: 1727–1743
9 Sharp G C, Kandasamy N, Singh H, Folkert M. Phys. Med. Biol., 2007, **52**: 5771–5783
10 XU Fang, Mueller K. IEEE Transactions on Nuclear Science, 2005, **52**(3): 654–663